Fusion Science and Technology

ISSN: 1536-1055 (Print) 1943-7641 (Online) Journal homepage: http://www.tandfonline.com/loi/ufst20

Incorporating Beam Attenuation Calculations into an Integrated Data Analysis Model for Ion Effective Charge

M. D. Nornberg, D. J. Den Hartog & L. M. Reusch

To cite this article: M. D. Nornberg, D. J. Den Hartog & L. M. Reusch (2018): Incorporating Beam Attenuation Calculations into an Integrated Data Analysis Model for Ion Effective Charge, Fusion Science and Technology, DOI: 10.1080/15361055.2017.1387008

To link to this article: https://doi.org/10.1080/15361055.2017.1387008

Published online: 19 Jan 2018.

FUSION SCIENCE AND TECHNOLOGY

DOI: https://doi.org/10.1080/15361055.2017.1387008

Incorporating Beam Attenuation Calculations into an Integrated Data Analysis Model for Ion Effective Charge

M. D. Nornberg,* D. J. Den Hartog, and L. M. Reusch

University of Wisconsin-Madison, Department of Physics, Madison, Wisconsin 53706

Received July 19, 2017
Accepted for Publication September 18, 2017

Abstract — *We have created a forward model for charge-exchange impurity density measurements that incorporates neutral beam attenuation measurements self-consistently for the purpose of determining the ion-effective charge Z_{eff}. The model is constructed within an integrated data analysis framework to include a self-consistent calculation of neutral beam attenuation due to multiple impurity species into the measurement of a single impurity density. The model includes measurements of the beam Doppler-shift spectrum and shine-through particle flux to determine the neutral beam particle density which is attenuated by ion collisions. Synthetic data are generated from the diagnostic forward model using statistical and calibration uncertainties. These "noisy" data are used in the analysis to evaluate how accurately Z_{eff} is determined. Methods of experimental design are employed to calculate the information gained from different diagnostic combinations. The analysis shows that while attenuation measurements alone do not provide a unique impurity density measurement in the case of a multispecies inhomogeneous plasma, they do provide an effective measurement of the Z_{eff} profile and place constraints on the impurity density profiles.*

Keywords — *Integrated data analysis, experimental design, ion-effective charge.*

Note — *Some figures may be in color only in the electronic version.*

I. INTRODUCTION: QUANTIFYING THE UNCERTAINTY IN CHARGE-EXCHANGE IMPURITY DENSITY MEASUREMENTS

Quantifying the impurity content of fusion-grade plasmas is a difficult, though critical, measurement. The effective ion charge Z_{eff}, a measure of the net impurity content of the plasma, is needed to quantify the resistive dissipation of currents in the plasma and to quantify the net radiative losses due to continuum emission. Conflicting values are often inferred from the use of single diagnostics, but the use of an integrated approach to multidiagnostic inferences of Z_{eff} can be crucial in identifying the systematic effects that lead to these contradictory results. A useful approach is to combine diagnostics that provide a useful lower bound on Z_{eff} through individual impurity density measurements, such as charge-exchange recombination spectroscopy (CHERS), with diagnostics that provide a combined measure of the impurity content such as brightness measurements of continuum emission in the visible or soft–X-ray (SXR) range. Research on the Madison Symmetric Torus (MST) has concentrated on using this approach to combine diagnostic information from CHERS impurity density measurements with brightness measurements from a SXR tomography system to determine the profile of Z_{eff} in enhanced-confinement plasmas.[1]

Inferring the density of particular impurity charge states from CHERS emission measurements is a challenging procedure. Local emission from impurity ions is generated by injecting a beam of hydrogen atoms into the plasma at high velocity to donate an electron via charge transfer.[2,3] This donated electron typically enters an excited state of the impurity ion and relaxes down to the ground state via spontaneous emission. The emission from a particular transition in this cascade at wavelength λ is quantified as

*E-mail: mdnornberg@wisc.edu

$$\varepsilon_{CHERS} = \frac{hc}{4\pi\lambda} \sum_j \left\langle \sigma^{j,\lambda}_{CHERS} v_b \right\rangle n_b^j n_z \ , \tag{1}$$

where

$\left\langle \sigma^{j,\lambda}_{CHERS} v_b \right\rangle$ = rate coefficient for the collision-induced emission (including the appropriate branching fraction)

n_b^j = beam particle densities of each of the E_j energy components

n_z = impurity density.

One determines the impurity density from knowledge of the rate coefficients and the beam particle densities. Neutral beams traversing magnetically confined plasmas are attenuated, however, by collisions with plasma ions. The beam-stopping cross sections due to collisions with nonhydrogenic ions (both ionization and charge-exchange) scale as[4,5]

$$\sigma_{stopping} \sim Z \times f(E/Z) \times 10^{20}\,\mathrm{m}^2 \ , \tag{2}$$

where $f(E/Z)$ is an empirical fit function indicating that the higher-Z impurity ions can attenuate a beam significantly for typically observed concentrations. Since the beam particle density depends on the net impurity content of the plasma, inferring the density of an individual charge state of a particular impurity species becomes an inherently recursive process. Usually this recursion is handled by iteration, but it quickly becomes difficult to correctly propagate uncertainties to the reported measurement.

This procedure can be simplified by assuming that the impurities are uniformly distributed[6] or by assuming that a single impurity species, e.g., carbon, is the dominant contributor to both the ion-effective charge

$$Z_{eff} = \frac{\sum_i Z_i^2 n_i}{\sum_i Z_i n_i} = \sum_i \frac{Z_i^2 n_i}{n_e} \tag{3}$$

and the beam attenuation. This second approach is justified for machines with graphite plasma–facing surfaces and strong gettering to remove oxygen, but the presence of metallic impurities in metal-walled machines and impurity seeding in the edge can make significant contributions to Z_{eff} as well. These circumstances have been addressed by providing a coincident measurement of the Doppler-shifted H_α emission[7,8] which is also proportional to the beam particle density for each energy component of the beam. Absent these coincident measurements, a model of the beam attenuation is necessary.

In this paper, we present a systematic method to create a single probabilistic analysis framework, an example of integrated data analysis[9–15] (IDA) that transparently and reliably incorporates all of the information available from beam Doppler-shift spectrum and beam particle flux measurements in addition to charge-exchange emission measurements in the inference of impurity charge-state density. This framework builds upon the modeling employed in Galante et al.[1] where SXR continuum emission measurements were incorporated into an inference of the effective charge profile $Z_{eff}(r)$ of reversed field pinch plasmas where the stochastic transport of ions from magnetic fluctuations is suppressed. In the discharges studied, the mechanism for impurity transport is known to be due to classical processes[16–18] which create hollow profiles from thermal screening. We take advantage of this prior knowledge to create parametric profiles for the impurities that are used self-consistently in the forward models for beam attenuation and for charge-exchange impurity emission. The hollowing of the impurity density profiles impacts the value of diagnostic information acquired from different points in the plasma; measurements near the mid-radius tend to be more important in quantifying the attenuation of the neutral beam particle density than measurements near the core. The value of these measurements is quantified by employing Bayesian techniques of experimental design to calculate the information each measurement adds to the final inference of the Z_{eff} profile.

II. METHOD: A FRAMEWORK FOR BEAM ATTENUATION CALCULATIONS

The framework we are using for the beam attenuation calculation starts with Bayes' Rule[9,19]:

$$p(\boldsymbol{\theta}|\mathbf{D}, I) = \frac{p(\mathbf{D}|\boldsymbol{\theta}, I)\, p(\boldsymbol{\theta}|I)}{p(\mathbf{D}|I)} \ , \tag{4}$$

where the posterior probability distribution of the parameters $\boldsymbol{\theta}$ is determined from the likelihood of measurements $\mathbf{D}$ and prior information I. The likelihood describes the probability of acquiring the observed data given a model with parameters $\boldsymbol{\theta}$ and is usually expressed as an analytical function which we will designate $\mathcal{L}(\mathbf{D}, \boldsymbol{\theta})$. But the likelihood is contingent on the probability that the parameters can take on certain values given background information I that is independent of the data acquired. The prior $p(\boldsymbol{\theta}|I)$ quantifies this contingent probability so that the probability that the set of parameters resides within the interval $(\boldsymbol{\theta}, \boldsymbol{\theta} + d\boldsymbol{\theta})$ can be written in differential form as $\pi(\boldsymbol{\theta})\, d\boldsymbol{\theta}$. The prior can constrain the parameter space searched when evaluating the likelihood by

enforcing criteria such as requiring amplitudes to be positive or limiting numerical values to the appropriate order of magnitude. The product of the likelihood and prior must be properly normalized so that $\int p(\boldsymbol{\theta}|\mathbf{D}, I)\, d\boldsymbol{\theta} = 1$. The normalization constant $p(\mathbf{D}|I)$, which we will call $\mathcal{Z}$, is referred to as the evidence and can be calculated as

$$\mathcal{Z} = \int \mathcal{L}(\mathbf{D}, \boldsymbol{\theta})\, \pi(\boldsymbol{\theta})\, d\boldsymbol{\theta}\,. \tag{5}$$

The evidence is a critical quantity in model comparison[20] and the use of integration over the full probability space of a parameter is a procedure referred to as marginalization. It is used in isolating probability distributions for particular parameters and eliminating nuisance parameters from further consideration.[9,19]

The parameterized model of impurity density profiles is based on the following pieces of information. First, we know from prior work that impurity transport can be described by classical collisional processes in these discharges[16–18]: impurities are expelled from the core by thermal screening. This effect motivates using a parameterized profile for each impurity density that creates a flat core region with an edge (defined by the two parameters α and β) with an additional Gaussian-shaped increment of amplitude δn_z located in the region of the mid-radius, specified by δr, of width Δr. For each impurity charge state z, the model density profile is

$$n_z(r, \boldsymbol{\theta}_z) = \frac{n_z^0}{[1 - (r/a)^{\alpha}]^{\beta}} + \frac{\delta n_z}{\sqrt{2\pi}(\Delta r/a)} \times \exp\left[-\frac{1}{2}\left(\frac{r - \delta r}{\Delta r}\right)^2\right], \tag{6}$$

where $\boldsymbol{\theta}_z = \{\alpha, \beta, n_z^0, \delta n_z, \delta r, \Delta r\}$ parameterize each impurity density profile. To reduce the parameter space required to search, we assume that all of the impurities have the same profile parameters with impurity-specific densities n_z^0 and δn_z. Based on prior observations, we also assume that all of the core low-Z impurity densities are proportional ($n_{O^{+8}} = 0.9\, n_{C^{6+}}$, $n_{N^{+7}} = 0.3\, n_{C^{6+}}$, and $n_{B^{+5}} = 0.3\, n_{C^{6+}}$) and the different core aluminum charge-state densities are in approximate coronal equilibrium.[21] This first assumption is supported by the hypothesis that the oxygen and nitrogen impurities are due to residual atmospheric gases and that the carbon and boron are generated from oxygen impact on wall materials. Both hypotheses are used in prior work that successfully reconciled SXR-brightness measurements which are sensitive to recombination emission from the impurities.[1] With these assumptions, the full model consists of the eight parameters $\boldsymbol{\theta} = \left\{\alpha, \beta, n^0_{C^{6+}}, n^0_{Al^{11+}}, \delta n_{C^{6+}}, \delta n_{Al^{11+}}, \delta r, \Delta r\right\}$. Figure 1 shows a comparison of the impurity density profiles (solid lines) to the published measurements for the ensemble averages.[16–18,21]

II.A. Establishing the Prior Probability Distribution

To establish bounds for the magnitude of the core impurity densities $n^0_{C^{6+}}$ and $n^0_{Al^{11+}}$ we define what constitutes an impurity. These discharges use deuterium fuel for plasmas. Typical observed charge-state densities of all other ions are no larger than 1%. For the purpose of establishing a range for the prior distribution, we assume that if the density of the particular ion charge-state species exceeds 10% it can no longer reasonably be called an impurity for the purposes of this analysis. For a lower bound, we can consider the mean free path of a beam atom for collisions with impurities of concentration $c_z = n_z/n_e$ using Eq. (2). For low-Z to mid-Z impurities ($Z \sim 10$) in a plasma with density $10^{19}\,\mathrm{m}^{-3}$ the mean free path is about

$$\lambda_{\mathrm{mfp}} = \frac{1}{n_z \sigma_{ii}} = \frac{1}{n_e c_z \sigma_{ii}} \sim \frac{1\ \mathrm{m}}{c_z}\,. \tag{7}$$

For an impurity concentration of $c_z \sim 1 \times 10^{-4}$, the expected attenuation due to ion collisions becomes 1 part in 10^4 which is negligible. Equation 3 implies that at this concentration the impurity contributes about 10^{-2} to the ion-effective charge which is also negligible. The resulting prior assumption for the model is that the impurities have a concentration between 10^{-4} and 10^{-1}. If we were to consider

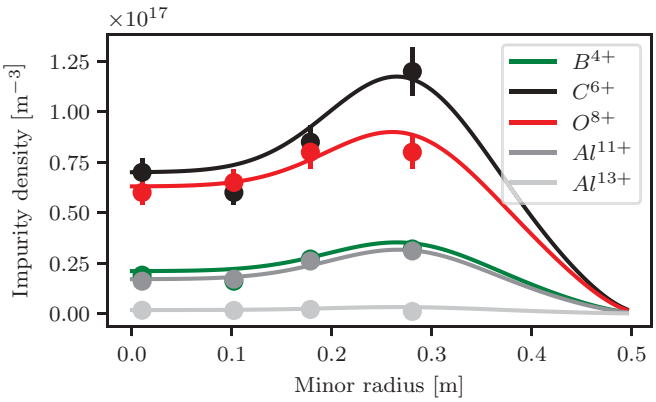

Fig. 1. Impurity density measurements from an ensemble of MST enhanced-confinement discharges with the model profiles overlaid (solid lines).

high-Z impurities like tungsten, the lower limit of the concentration would extend to ~10^{-6} under similar criteria.

The prior distribution for location parameters like δr are typically specified with a uniform distribution. The prior distribution for an amplitude parameter like n_z^0, however, is positive definite and the range of possible impurity concentrations spans four orders of magnitude. If we were to use a uniform prior distribution for this parameter, then a random sample of the distribution would tend to be biased toward higher densities. Typically, the prior distribution for an amplitude parameter can be specified as a logarithmic distribution function to avoid this biasing.[19] We employ a Monte Carlo computational method which draws random samples from the prior distributions for each of the parameters for use in evaluation of the likelihood of the measurements. Samples from the prior probability distributions for this analysis (indicated with a hat superscript) are drawn according to:

$$\widehat{\alpha} = X \qquad X \in [5.0, 14.0] \,,$$

$$\widehat{\beta} = X \qquad X \in [2.0, 18.0] \,,$$

$$\widehat{n_z^0} = 10^X \,\mathrm{m}^{-3} \qquad X \in [14.0, 18.0] \,,$$

$$\widehat{\delta n_z} = 10^X \,\mathrm{m}^{-3} \qquad X \in [14.0, 18.0] \,,$$

$$\widehat{\delta r} = X \,\mathrm{m} \qquad X \in [0.25, 0.45] \,,$$

and

$$\widehat{\Delta r} = X \,\mathrm{m} \qquad X \in [0.05, 0.25] \,, \tag{8}$$

where pseudo-random floating point numbers X are drawn uniformly from the indicated intervals.

Some of the diagnostic measurements included in the likelihood are not direct measurements of any of the parameters, but rather the particle density of the 50-kV diagnostic neutral beam (DNB) and emission from the beam which depends on the beam particle densities $n_b^j(\ell)$ for the three energy components j where ℓ is the distance the beam traverses through the plasma across the minor diameter of length $2a$ (see Fig. 2). As indicated in Eq. (2), the primary mechanism for beam attenuation is collisions with ions. Particularly important is quantifying the losses due to collisions with the majority ions. We assume as in the previous analysis that the electron density profile $n_e(r)$ is known from multichord interferometry measurements. For each randomly sampled set of parameters $\widehat{\boldsymbol{\theta}}$ we obtain a sample of impurity profiles $\widehat{n_z}(r) = n_z\left(r, \widehat{\boldsymbol{\theta}}\right)$ and determine

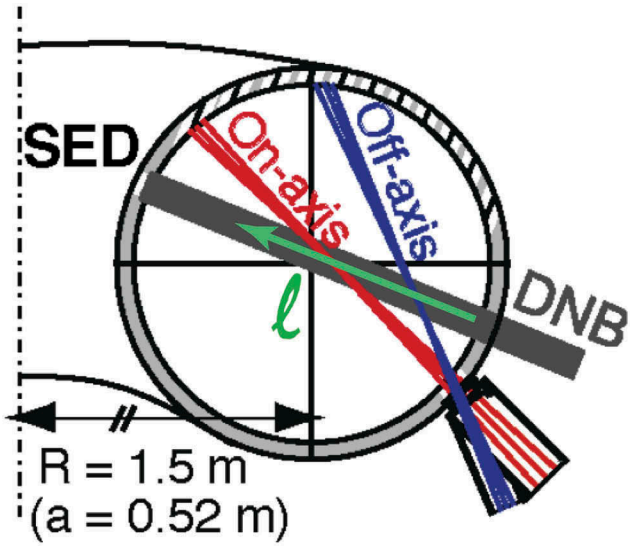

Fig. 2. Geometry of the 50-kV DNB. The beam is aligned radially and passes through the plasmas from the outboard to the inboard side. Attenuation due to collisional ionization and charge exchange reduces the beam particle density $n_b^j(\ell)$ of each of the three energy components j at distance ℓ along the beam path. Three measurements are used to provide local constraints on the beam particle density. The SED measures the flux of beam particles after they have traversed the poloidal cross section of the plasma. Two spectrometer views, one on the magnetic axis (red) and one placed at the mid-radius (blue), provide measurements of the Doppler-shifted H_α spectrum of the three beam energy components (adapted from Ref. 22).

the majority ion density profile $\widehat{n_i}(r) = n_i\left(r, \widehat{\boldsymbol{\theta}}\right)$ through quasi-neutrality. From this set of sample profiles, the attenuation of the DNB along the path length ℓ yields a beam particle density profile:

$$\widehat{n_b^j}(\ell) = n_b^j(0) \int_0^{2a} d\ell \, \exp\left[- \sum_z \widehat{n_z}(\ell) \, \sigma_z(E_j) \right] \,, \tag{9}$$

where $n_b^j(0)$ is the injected beam particle density for each of the energy components j determined from measurements of the beam current and prior calibration, and $\sigma_z(E_j)$ is the stopping cross section for impurity charge state z. The stopping cross sections depend primarily on the beam energy E_j as indicated in Eq. (2).

In order to visualize the probability distribution of the profiles of quantities derived from the model parameters, we use a straightforward Monte Carlo analysis to produce random samples $\widehat{\boldsymbol{\theta}}$ according to Eq. (8) and create sample ensembles of the impurity density profiles and beam particle density profiles. Credibility regions are calculated from the percentiles of the sampled function in

Eq. (6) for the impurity density profiles and Eq. (9) for the beam particle density profile. A credible region $[F_1(r), F_2(r)]$ is defined for a function $f\left(r, \widehat{\boldsymbol{\theta}}\right)$ such that

$$p(f(r, \boldsymbol{\theta}) \in [F_1(r), F_2(r)]) = \mathcal{C} \times 100 \ ,$$

where $\mathcal{C}$ is some percentage of the total probability. The interval is chosen so that $\mathcal{C}/2$ percent of values are greater than $F_1(r)$ and $100 - \mathcal{C}/2$ percent of values are greater than $F_2(r)$ which centers the region on the median value at each r. We choose values of 68%, 95%, 99.7% for $\mathcal{C}$ corresponding to one to three standard deviations. The reason for choosing multiple probability regions is to highlight where knowledge of $f(r, \boldsymbol{\theta})$ becomes more precise (peaked) due to experimental observations compared with where it remains highly uncertain (flat).

The feasible range of impurity densities and beam particle densities within the range of parameters established in Eq. (8) are depicted in Fig. 3 using credibility regions that show that the prior impurity distributions have a flat profile on a logarithmic scale while the beam particle densities tend to be skewed to higher values.

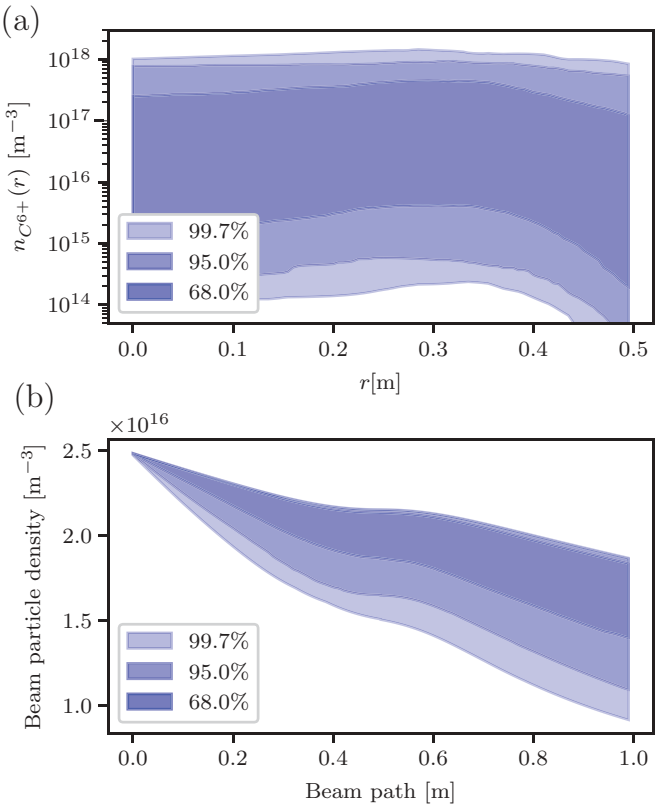

Fig. 3. (a) Prior probability distribution of the C^{6+} density profile depicted using the indicated credibility regions and (b) the prior probability distribution of the neutral beam particle density (summed over all three energy components).

II.B. Likelihood for Beam Particle Flux and Emission Measurements

We will employ several measurements sensitive to the neutral beam particle density available on the MST depicted in Fig. 2 as part of the likelihood. The first is a secondary electron detector[23] (SED), or shine-through detector, which measures the beam particle flux after it traverses the plasma. From the sample parameters $\widehat{\boldsymbol{\theta}}$ we model the measured particle flux as

$$\widehat{\Gamma_{\text{SED}}} = \sum_j \widehat{n_b^j}(\ell = 2a) v_b^j \ . \tag{10}$$

The uncertainty in the SED measurement is largely due to calibration uncertainty which is determined from fitting to data acquired when the beam is fired into vacuum. There are sufficient calibration data to assume that the variability in the measurement can be characterized as a Gaussian distribution with a standard deviation σ_{SED}. The estimated relative uncertainty is 10%.

The other measurements are beam Doppler-shift spectroscopy (DSS) measurements with views at the magnetic axis and at the outboard half-radius. The collisionally induced emission of Doppler-shifted H_α light for each beam energy component j is

$$\widehat{\varepsilon_{\text{H}_\alpha}^j} = \frac{A_{32}}{A_{32} + A_{31}} \frac{hc}{4\pi\lambda_{\text{H}_\alpha}^j} \sum_z \left\langle \sigma_{\text{H}_\alpha} v_{beam}^j \right\rangle \widehat{n_b^j} \widehat{n_z} \ , \tag{11}$$

where the z-summation is over all of the ion species and A_{ij} are the Einstein coefficients for spontaneous emission from level i to j. This model assumes that the $n = 3$ level is primarily populated by collisional excitation of ground-state atoms and depopulated by spontaneous emission. The plasma we are studying is sufficiently rarefied that collisional deexcitation and photon reabsorption are negligible processes. An example measurement of the spectral radiance $L_{\text{H}_\alpha}^j = \int dw \varepsilon_{\text{H}_\alpha}^j$ (the line-integrated emission from the intersection of the spectrometer line of sight with the neutral beam) from Doppler-shifted H_α emission is shown in Fig. 4. The photon counts are usually sufficiently large that the dominant uncertainty σ_{H_α} is a calibration uncertainty of about 5%.

Since the calibration data for each diagnostic provide an estimate of both the calibration constant and its variance, according to the principle of maximum entropy the appropriate probability distribution to use for the likelihood is a Gaussian distribution.[24] The six radiance measurements

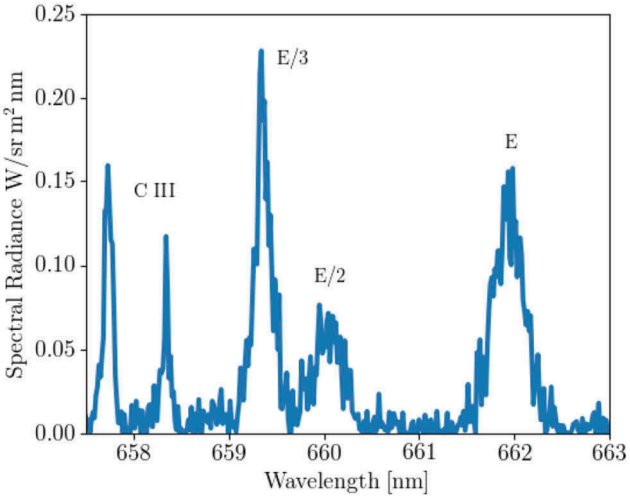

Fig. 4. An example of on-axis beam DSS. The two left-most peaks are due to edge carbon emission from the plasma while the three right-most peaks are the Doppler-shifted H_α emission from the three beam energy components.

$L_{H_\alpha}^{\text{meas}_j}$ and the SED particle flux measurement $\Gamma_{\text{SED}}^{\text{meas}}$ are incorporated as data $\mathbf{D}$ in the calculation of the likelihood

$$\mathcal{L}(\mathbf{D},\widehat{\boldsymbol{\theta}}) = \mathcal{L}_{\text{SED}} \times \mathcal{L}_{H_\alpha} \,, \tag{12}$$

$$\mathcal{L}_{\text{SED}} = \frac{1}{\sqrt{2\pi\sigma_{\text{SED}}^2}} \times \exp\left[-\frac{1}{2}\left(\frac{\Gamma_{\text{SED}}^{\text{meas}} - \widehat{\Gamma_{\text{SED}}}}{\sigma_{\text{SED}}}\right)^2\right] , \tag{13}$$

and

$$\mathcal{L}_{H_\alpha} = \frac{1}{\sqrt{2\pi\prod_j \left(\sigma_{H_\alpha}^j\right)^2}} \times \exp\left[-\frac{1}{2}\sum_j \left(\frac{L_{H_\alpha}^{\text{meas}_j} - \widehat{L_{H_\alpha}^j}}{\sigma_{H_\alpha}^j}\right)^2\right] . \tag{14}$$

III. RESULTS: CALCULATING POSTERIOR INFERENCES USING NESTED SAMPLING

Since we are developing a new analysis technique for interpreting the CHERS data, we will begin by working with synthetic data calculated from the ensemble-averaged impurity density measurements shown in Fig. 1. This way, we can compare the analysis results determined from calculations using data randomly drawn from a known distribution based on the measurement uncertainties with the true impurity density profiles.

To infer the appropriate beam particle density in charge-exchange recombination measurements and the implied ion-effective charge profile for the plasma, we need to construct appropriately weighted samples of the posterior $p(\boldsymbol{\theta}|\mathbf{D},I)$ using the prior described in Eq. (8) and the likelihoods described in Eqs. (12), (13), and (14). We anticipate that there are many possible combinations of impurity density profiles that can result in the measurements $\mathbf{D}$ so the posterior distribution may be very broad with significant correlation among the parameters. We are also interested in quantifying the information content of each of the diagnostic measurements. As such, we choose to employ the nested sampling technique[20] via the pyMultiNest package.[25,26]

Nested sampling seeks to determine the evidence $\mathcal{Z} = p(\mathbf{D}|I)$ by sampling within the volume of the prior probability distribution constrained by increasing values of the likelihood. The algorithm balances the need to span the entire prior probability volume with the desire to find the region of maximum likelihood quickly. The calculation generates a set of samples $\widehat{\boldsymbol{\theta}}_i$ from the posterior $p(\boldsymbol{\theta}|\mathbf{D},I)$ and weights w_i which can be used to calculate the evidence:

$$\mathcal{Z} \approx \sum_i w_i \mathcal{L}\left(\mathbf{D},\widehat{\boldsymbol{\theta}}_i\right) . \tag{15}$$

The weighted samples are also used to determine posterior inferences of the probability distributions for each of the impurity density profiles and the beam particle density profile. For instance, the average profile of the impurity charge-state density z can be calculated from the weighted samples as

$$\langle n_z(r,\boldsymbol{\theta})\rangle \approx \sum_i \frac{w_i}{\mathcal{Z}} \mathcal{L}\left(\mathbf{D},\widehat{\boldsymbol{\theta}}_i\right) n_z\left(r,\widehat{\boldsymbol{\theta}}_i\right) . \tag{16}$$

To express the shape of the posterior probability distribution of the profiles, we will again plot credibility regions as discussed in Sec. II.A, but now we will be using the weighted samples from the posterior probability distribution. Examples are shown in Fig. 5 using same three credibility values as before.

Note that although the on-axis beam particle density is determined to within 5% at 95% credibility, the C^{6+} particle density is only constrained to within an order of magnitude at 68% credibility. The beam particle density and emission

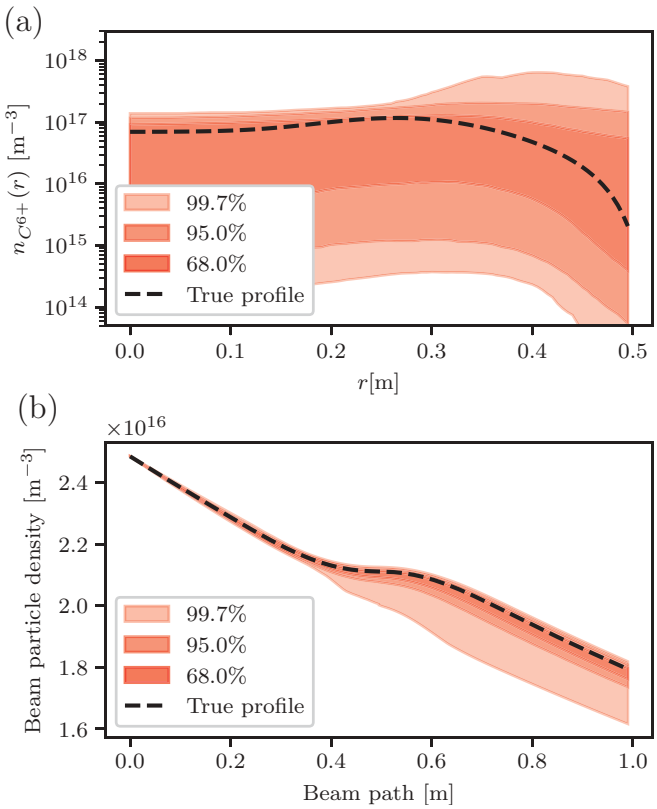

Fig. 5. Posterior probability distributions of (a) the C^{6+} density profile and (b) the neutral beam particle density (summed over all three energy components) constrained by measurements of the beam particle flux and Doppler-shifted H_α emission using Eqs. (13) and (14).

measurements do not provide precise information on any specific impurity, but the posterior inferences of the impurity densities are correlated such that an aggregate measure like Z_{eff} is more tightly constrained to within 25% in the 68% credibility region as seen in Fig. 6.

If we further constrain the solution by adding an on-axis C^{6+} CHERS radiance measurement to the likelihood calculation, we further constrain the parameter set and obtain a measurement of the on-axis C^{6+} density. The CHERS emission is determined from Eq. (1) using a Gaussian likelihood $\mathcal{L}_{\text{CHERS}}$ like Eqs. (13) and (14) since, again, the uncertainty is due primarily to calibration and fitting uncertainties. The relative uncertainty is about 10%. In Fig. 7, the posterior probability distribution $p(n_{C^{6+}}(r,\boldsymbol{\theta})|\mathbf{D},I)$ peaks significantly due to the constraint imposed by the likelihood of the CHERS measurement to the point where it can be well-approximated as a Gaussian distribution. The resulting analysis can be reported as the traditional most-likely estimate with an error bar indicating the estimate of the standard deviation, but doing so will discard the information obtained in inferring the most credible estimates of the entire C^{6+} profile contained in the full posterior distribution $p(\boldsymbol{\theta}|\mathbf{D},I)$.

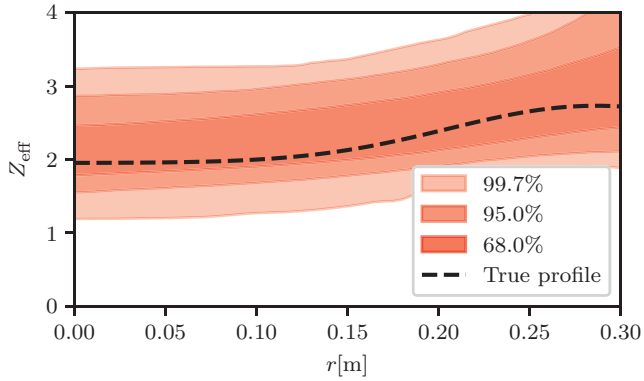

Fig. 6. Posterior probability distributions of the ion-effective charge profile using SED and both on-axis and off-axis DSS measurements.

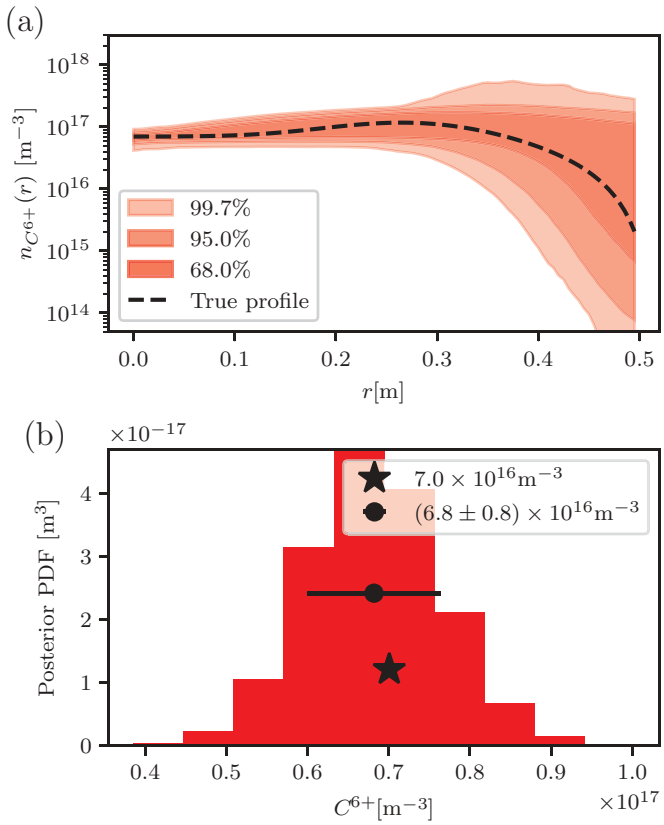

Fig. 7. Posterior probability distributions of (a) the C^{6+} density profile and (b) a histogram of the properly normalized posterior PDF for the core C^{6+} impurity density $p(n_{C^{6+}}(r=0,\boldsymbol{\theta})|\mathbf{D},I)$ showing that the posterior at $r=0$ is approximately Gaussian. The true core density used in generating the synthetic data is indicated (star) as well as an error bar based on the mean and standard deviation.

If we acquire additional data $\mathbf{D_2}$, then we can continue to use the calculated posterior from the previous data $p(\boldsymbol{\theta}|\mathbf{D}_1,I)$ in the following way. The likelihood distribution due to all of

the data is $p(\mathbf{D}_1, \mathbf{D}_2|\boldsymbol{\theta}, I) = p(\mathbf{D}_1|\boldsymbol{\theta}, I)p(\mathbf{D}_2|\mathbf{D}_1, \boldsymbol{\theta}, I)$. If $\mathbf{D}_1$ and $\mathbf{D}_2$ are logically independent, then $p(\mathbf{D}_2|\mathbf{D}_1, \boldsymbol{\theta}, I) = p(\mathbf{D}_2|\boldsymbol{\theta}, I)$ and $p(\mathbf{D}_1, \mathbf{D}_2|I) = p(\mathbf{D}_1|I)p(\mathbf{D}_2|I)$. The application of Bayes' Theorem in Eq. (4) gives the new posterior distribution as

$$p(\boldsymbol{\theta}|\mathbf{D}_1, \mathbf{D}_2, I) = \frac{p(\mathbf{D}_1, \mathbf{D}_2|\boldsymbol{\theta}, I)p(\boldsymbol{\theta}|I)}{p(\mathbf{D}_1, \mathbf{D}_2|I)} . \tag{17}$$

$$= \frac{p(\mathbf{D}_2|\boldsymbol{\theta}, I)}{p(\mathbf{D}_2|I)} \frac{p(\mathbf{D}_1|\boldsymbol{\theta}, I)p(\boldsymbol{\theta}|I)}{p(\mathbf{D}_1|\boldsymbol{\theta})} \tag{18}$$

and

$$= \frac{p(\mathbf{D}_2|\boldsymbol{\theta}, I)}{p(\mathbf{D}_2|I)} p(\boldsymbol{\theta}|\mathbf{D}_1, I) . \tag{19}$$

Equation 19 is equivalent to using the posterior determined from $\mathbf{D}_1$ as the prior distribution in a subsequent calculation incorporating the likelihood for data $\mathbf{D}_2$. Thus, the procedure for including additional data in determining the best estimates of the parameters $\boldsymbol{\theta}$ is quite modular and facilitates the further integration of additional diagnostics.

IV. DISCUSSION: QUANTIFYING THE INFORMATION GAIN

Each of the diagnostic signals incorporated into the likelihood calculation provides a different type of constraint on the inferred beam particle density profile. The constraint from particular diagnostics can be quantified by performing the same analysis without that diagnostic. Figure 8 shows the inferred beam particle density profile if we use only the SED and on-axis DSS measurements in Eqs. (13) and (14). Note how the credibility region grows significantly without the information from the off-axis DSS measurements. In fact, since the model allows for impurity particle transport to cause peaking of the impurity density profiles at the mid-radius it is clear that the off-axis spectrum measurement is quite important in obtaining a small uncertainty on the beam particle density across the entire profile. A comparison of Fig. 8b with Fig. 5b shows that we achieve a similar level of constraint even without the on-axis spectrum measurement.

We can quantify how valuable each diagnostic measurement is to the analysis by calculating how much information is gained in going from the prior probability distribution to the posterior. This expected information gain (EIG) is equated to the reduction in the Shannon entropy (or Kullback-Liebler divergence) between the two distributions[9,19]:

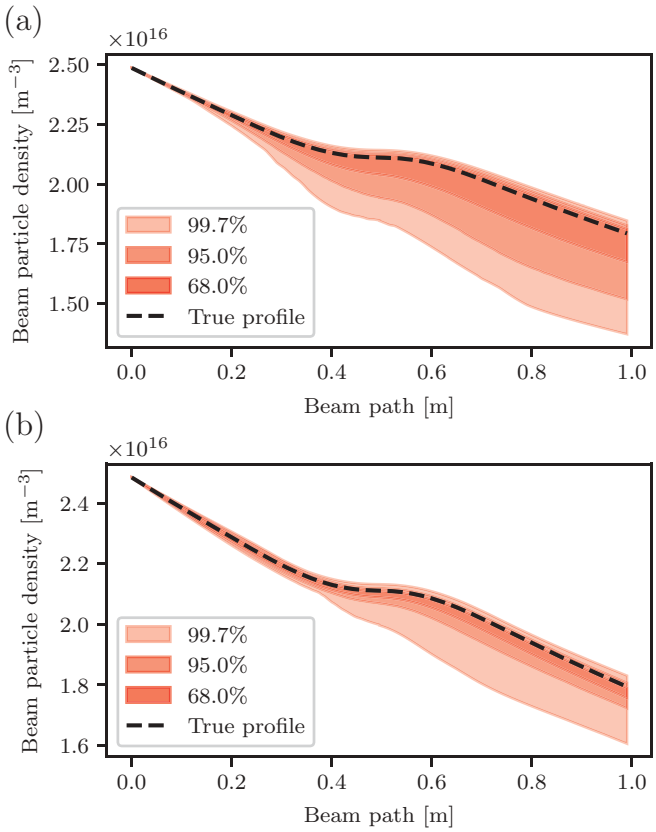

Fig. 8. Posterior probability distribution of the neutral beam particle density using a likelihood constructed from (a) SED and on-axis DSS measurements and (b) SED and off-axis DSS measurements.

$$\mathrm{EIG} = \int p(\boldsymbol{\theta}|\mathbf{D}, I) \log\left(\frac{p(\boldsymbol{\theta}|\mathbf{D}, I)}{p(\boldsymbol{\theta}|I)}\right)$$

$$\approx \sum_i \frac{w_i}{\mathcal{Z}} p\left(\mathbf{D}|\widehat{\boldsymbol{\theta}}_i, I\right) \log \frac{p\left(\mathbf{D}|\widehat{\boldsymbol{\theta}}_i, I\right)}{\mathcal{Z}} , \tag{20}$$

where the weights w_i and parameter samples $\widehat{\boldsymbol{\theta}}$ are calculated from the nested sampling algorithm and the evidence $\mathcal{Z}$ is calculated from Eq. (15). A table of EIG values for several diagnostic combinations is presented in Table I. The calculation uses base-2 logarithms so that the EIG is expressed in bits. Note that the information gain from the off-axis spectrum measurement is greater than the on-axis measurement as determined earlier by comparisons of the credible range of beam particle density profiles in Fig. 8.

Note in particular that we do not learn much more about the impurity density profiles or Z_{eff} from an isolated measurement of the beam particle flux to the wall. The model provides sufficient flexibility that there are many possible combinations of impurity profiles that could result in one particular measurement of

TABLE I

EIG with Each Combination of Diagnostic Information

Diagnostics	Secondary Electron Detector	Secondary Electron Detector and On-Axis Doppler-Shift Spectroscopy	Secondary Electron Detector and On-Axis Doppler-Shift Spectroscopy	Secondary Electron Detector and Doppler-Shift Spectroscopy	Secondary Electron Detector, Doppler-Shift Spectroscopy, and Charge-Exchange Recombination Spectroscopy
EIG (bits)	1.7	12.2	14.1	22.7	34.6

the particle flux making its inclusion in the diagnostic data **D** inconsequential. This result is consistent with the general understanding of the limitations of using beam attenuation measurements alone as a means of determining Z_{eff} (see Hutchinson[5] for an excellent discussion). The additional information acquired from the beam DSS measurements provides an acceptable constraint on the beam particle density for inferring the point measurement of the impurity density as is the case with the traditional CHERS emission measurement, but since we have a model for the profile, there is also a valid inference for a credible range across the entire plasma. In Fig. 7 this constraint is apparent across most of the core of the plasma, but it starts to widen significantly in the edge where the model allows for larger variability due to lack of data to constrain it.

V. CONCLUSION

Following the IDA methodology, we have created a self-consistent calculation of the attenuation of a 50-kV DNB used in impurity density measurements through charge-exchange recombination emission. Measurements of the beam shine-through particle flux and beam DSS provide sufficient constraints to infer the Z_{eff} profile as demonstrated from performing the analysis with synthetic data. The resulting posterior probability distribution function (PDF) contains all of the covariances between the densities of different impurities so as to make them consistent with the inferred beam attenuation. In addition to providing an inference of the local C^{6+} density, the analysis provides an inference for the entire set of impurity density profiles. The information available in the posterior distribution is modular; it is part of a larger analysis that can incorporate other diagnostic measurements like SXR emission to provide further constraints. An analysis of the EIG from different diagnostic combinations highlights the importance of including off-axis beam DSS measurements due to the outward transport of impurities which aids in evaluating where to concentrate diagnostic resources to quantify the ion-effective charge profile.

Acknowledgments

This material is based upon work supported by the U.S. Department of Energy Office of Science, Office of Fusion Energy Sciences program under awards DE-FC02-05ER54814 and DE-SC0015474.

ORCID

M. D. Nornberg http://orcid.org/0000-0003-1786-4190

References

1. M. E. GALANTE et al., "Determination of Z_{eff} by Integrating Measurements from X-Ray Tomography and Charge Exchange Recombination Spectroscopy," *Nucl. Fusion*, **55,** *12*, 123016 (2015); https://doi.org/10.1088/0029-5515/55/12/123016.
2. R. C. ISLER, "A Review of Charge-Exchange Spectroscopy and Applications to Fusion Plasmas," *Physica. Scripta.*, **35,** *5*, 650 (1987); https://doi.org/10.1088/0031-8949/35/5/007.
3. R. J. FONCK, D. S. DARROW, and K. P. JAEHNIG, "Determination of Plasma-Ion Velocity Distribution Via Charge-Exchange Recombination Spectroscopy," *Phys. Rev. A*, **29**, 3288 (1984); https://doi.org/10.1103/PhysRevA.29.3288.
4. R. K. JANEV, C. D. BOLEY, and D. E. POST, "Penetration of Energetic Neutral Beams into Fusion Plasmas," *Nucl. Fusion*, **29,** *12*, 2125 (1989); https://doi.org/10.1088/0029-5515/29/12/006.

5. I. H. HUTCHINSON, *Principles of Plasma Diagnostics*, 2nd ed. Cambridge University Press, Cambridge, United Kingdom (2002).

6. M.-C. HUBLET et al., "Attenuation Measurement of an Atomic Hydrogen Beam as a Diagnostic Technique to Determine the Light Impurity Content of a Plasma," *Plasma Phys. Control. Fusion*, **30,** *7*, 829 (1988); https://doi.org/10.1088/0741-3335/30/7/002.

7. R. J. E. JASPERS et al., "Validation of the ITER CXRS Design by Tests on TEXTOR," *Rev. Sci. Instr.*, **79,** *10*, 10F526 (2008); https://doi.org/10.1063/1.2979874.

8. I. O. BESPAMYATNOV et al., "An Integrated Charge Exchange Recombination Spectroscopy/Beam Emission Spectroscopy Diagnostic for Alcator C-Mod Tokamak," *Rev. Sci. Instr.*, **81,** *10*, 10D709 (2010); https://doi.org/10.1063/1.3475707.

9. U. VON TOUSSAINT, "Bayesian Inference in Physics," *Rev. Mod. Phys.*, **83**, 943 (2011); https://doi.org/10.1103/RevModPhys.83.943.

10. R. FISCHER and A. DINKLAGE, "Integrated Data Analysis of Fusion Diagnostics by Means of the Bayesian Probability Theory," *Rev. Sci. Instr.*, **75,** *10*, 4237 (2004); https://doi.org/10.1063/1.1787607.

11. J. SVENSSON and A. WERNER, "Large Scale Bayesian Data Analysis for Nuclear Fusion Experiments," *Proc. 2007 IEEE Int. Symp. Intelligent Signal Processing*, Alcala de Henares, Spain, October 3–5, 2007; https://doi.org/10.1109/WISP.2007.4447579.

12. R. FISCHER et al., "Probabilistic Lithium Beam Data Analysis," *Plasma Phys. Control. Fusion*, **50,** *8*, 085009 (2008); https://doi.org/10.1088/0741-3335/50/8/085009.

13. G. VERDOOLAEGE, R. FISCHER, and G. VAN OOST, "Potential of a Bayesian Integrated Determination of the Ion Effective Charge Via Bremsstrahlung and Charge Exchange Spectroscopy in Tokamak Plasmas," *IEEE Trans. Plasma Sci.*, **38,** *11*, 3168 (2010); https://doi.org/10.1109/TPS.2010.2071884.

14. R. FISCHER et al., "Integrated Data Analysis of Profile Diagnostics at ASDEX Upgrade," *Fusion Sci. Tech.*, **58,** *2*, 675 (2010); https://doi.org/10.13182/FST10-110.

15. S. K. RATHGEBER et al., "Estimation of Profiles of the Effective Ion Charge at ASDEX Upgrade with Integrated Data Analysis," *Plasma Phys. Control. Fusion*, **52,** *9*, 095008 (2010); https://doi.org/10.1088/0741-3335/52/9/095008.

16. S. T. A. KUMAR et al., "Classical Impurity Ion Confinement in a Toroidal Magnetized Fusion Plasma," *Phys. Rev. Lett.*, **108**, 125006 (2012); https://doi.org/10.1103/PhysRevLett.108.125006.

17. S. T. A. KUMAR et al., "Classical Confinement and Outward Convection of Impurity Ions in the MST RFP," *Phys. Plasmas*, **19,** *5*, 056121 (2012); https://doi.org/10.1063/1.4718310.

18. T. BARBUI et al., "Impurity Transport Studies in the Madison Symmetric Torus Reversed-Field Pinch During Standard and Pulsed Poloidal Current Drive Regimes," *Plasma Phys. Control. Fusion*, **56,** *7*, 075012 (2014); https://doi.org/10.1088/0741-3335/56/7/075012.

19. D. SIVIA and J. SKILLING, *Data Analysis: A Bayesian Tutorial*, Oxford University Press, Oxford, United Kingdom (2006).

20. J. SKILLING, "Nested Sampling for General Bayesian Computation," *Bayesian Anal.*, **1,** *4*, 833 (2006); https://doi.org/10.1214/06-BA127.

21. S. T. A. KUMAR et al., "High Resolution Charge-Exchange Spectroscopic Measurements of Aluminum Impurity Ions in a High Temperature Plasma," *Plasma Phys. Control. Fusion*, **54,** *1*, 012002 (2012); https://doi.org/10.1088/0741-3335/54/1/012002.

22. J. KO and J. KLABACHA, "Improved Spectral Analysis for the Motional Stark Effect Diagnostic," *Rev. Sci. Instr.*, **83,** *10*, 10D513 (2012); https://doi.org/10.1063/1.4733546.

23. J. H. FOOTE, A. W. MOLVIK, and W. C. TURNER, "Plasma Measurements from Neutral-Beam Attenuation," *Rev. Sci. Instr.*, **54,** *8*, 928 (1983); https://doi.org/10.1063/1.1137504.

24. E. T. JAYNES and L. BRETTHORST, *Probability Theory, the Logic of Science*, Oxford University Press, Oxford, United Kingdom (2003).

25. J. BUCHNER et al., "X-Ray Spectral Modelling of the AGN Obscuring Region in the CDFS: Bayesian Model Selection and Catalogue," *Astro. Astrophys.*, **564**, A125 (2014); https://doi.org/10.1051/0004-6361/201322971.

26. F. FEROZ, M. P. HOBSON, and M. BRIDGES, "MultiNest: An Efficient and Robust Bayesian Inference Tool for Cosmology and Particle Physics," *Mon. Not. R. Astron. Soc.*, **398,** *4*, 1601 (2009); https://doi.org/10.1111/j.1365-2966.2009.14548.x.